Dynamic modeling of cusp ion structures

H. J. Connor,[1] J. Raeder,[1] and K. J. Trattner[2]

Received 29 September 2011; revised 23 January 2012; accepted 15 February 2012; published 5 April 2012.

[1] Dispersed ion structures observed near the magnetosphere cusps have long been used to infer locations and properties of reconnection at the Earth's magnetopause. However, observations are often difficult to interpret since spacecraft move relative to a cusp ion structure, creating temporal and spatial ambiguity in the observations. Models of cusp ion structures are also limited to the cases during stable solar wind and interplanetary magnetic field (IMF) because empirical models are used to obtain the Earth's electromagnetic fields. We introduce a new model of a cusp ion structure by using the Liouville theorem particle tracer (LTPT) with the OpenGGCM 3D global MHD model. The OpenGGCM produces time-dependent magnetospheric electromagnetic fields under various solar wind and IMF conditions, while the LTPT traces test particles backward from an observation point to the magnetosheath to map the phase space density and construct an energy-time spectrogram. This allows our model to study cusp ion structures under dynamic solar wind and IMF conditions. In this paper, we first test our model's capability by reconstructing the cusp ion structures observed from three cusp-crossing events of Cluster and Polar satellites. We show that the model reproduces various observed ion structures, such as normal dispersion, reverse dispersion, double dispersions, and stepped dispersion. We then show that the cusp structures observed by Cluster on 23 September 2004 and on 23 August 2003 are temporal structures caused by a sudden increase of solar wind dynamic pressure and various reconnection rates, respectively. We also show that the stepped dispersion observed by Polar on 25 August 1998 is not only spatial but also temporal, caused by two different subsolar reconnection sites during a change of the IMF clock angle. In addition, we find that the ions entering the cusp often cross the magnetopause far away from the reconnection site, even though the reconnection is the cause of precipitation, and that the magnetic configuration of the magnetosheath is also sometimes a cause of energy dispersion in a cusp structure.

Citation: Connor, H. J., J. Raeder, and K. J. Trattner (2012), Dynamic modeling of cusp ion structures, *J. Geophys. Res.*, *117*, A04203, doi:10.1029/2011JA017203.

1. Introduction

[2] The Earth's magnetic cusps are funnel-like regions where solar wind plasma can penetrate close to the Earth. The concept of the cusp was first introduced by *Chapman and Ferraro* [1931a, 1931b], who defined the magnetopause as a perfect conductor to prevent solar wind plasma from penetrating into the magnetosphere. They predicted two singular points called cusps, one in each hemisphere, where solar wind plasma could enter into the magnetosphere. Unlike the Chapman-Ferraro prediction, solar wind-like plasma is observed over broad regions, not just at a singular point at each hemisphere. Therefore, the magnetopause is not a perfect conductor, thus allowing magnetic reconnection between the interplanetary magnetic field (IMF) and the Earth's magnetic field [*Dungey*, 1958, 1961].

[3] Cusp ion structures, i.e., energy versus time (or energy versus latitude) spectrograms of cusp ions, are closely related to dayside reconnection. Reconnection between the IMFs and the Earth's magnetic fields creates open magnetic field lines which are convected by magnetic tension and magnetosheath flow. Magnetosheath plasma particles precipitate into the cusp along the open field lines. The different field-aligned velocities of the precipitating magnetosheath ions result in different arrival times in the low-altitude cusp. This velocity filter effect [*Rosenbauer et al.*, 1975; *Shelley et al.*, 1976; *Reiff et al.*, 1977; *Hill and Reiff*, 1977] in combination with convection of the open field lines by the magnetosheath plasma produces a unique cusp structure in energy-time or energy-latitude spectrograms.

[4] For southward IMF conditions and an equatorward reconnection location, higher-energy ions arrive earlier at lower magnetic latitudes in the cusp while lower-energy ions arrive at higher latitudes. In contrast, during northward IMF conditions and a lobe reconnection location a reverse ion

[1]Space Science Center, University of New Hampshire, Durham, New Hampshire, USA.
[2]Lockheed-Martin Advanced Technology Center, Palo Alto, California, USA.

0148-0227/12/2011JA017203

energy dispersion is observed. Unlike these two simple cases, cusp ion structures are often complicated, and more detailed studies are needed to understand the relation between cusp ion structures and reconnection.

[5] Many observational studies of cusp ion structures have identified properties and locations of dayside reconnection. Cusp ion structures are interpreted as either temporal or spatial structures, related to temporal or spatial variation of reconnection. *Lockwood and Smith* [1989, 1990, 1994] suggested that multiple dispersions or steps in a cusp structure are temporal structures caused by low or no reconnection rate between reconnection pulses. *Trattner et al.* [2008] presented observations from two Cluster satellites in which the poleward satellite observes two step-up structures a few minutes later than the equatorward satellite. The propagation speed of these structures is comparable with the convection speed observed by the Super Dual Auroral Radar Network (SuperDARN), suggesting that the step-up structures are temporal structures.

[6] However, the variation of the reconnection rate is not the only possible reason for multiple dispersions. *Onsager et al.* [1995] studied observations from two Dynamics Explorer satellites that passed the cusp ~20 min apart. Both satellites observe double dispersions despite the time separation, suggesting that the double dispersion structure is spatial. Spatial cusp structures are also discussed in a study by *Trattner et al.* [2005], who combined a double cusp event observed by the Cluster satellites with simultaneous ionospheric convection observations by the SuperDARN radars. For this particular event, the two cusp ion-energy dispersions aligned with the two ionospheric convection cells, which was interpreted as a spatial phenomenon. *Escoubet et al.* [2008a] also supported the idea of multiple reconnection sites by showing that cusp ion structures observed by Cluster are composed of ions from two different sources on the magnetopause: component reconnection near a subsolar point and antiparallel reconnection near the high-latitude duskside of the magnetopause.

[7] The spatial or temporal nature of cusp structures is not always easy to distinguish because of the temporal and spatial ambiguities of the orbiting single satellites. To separate spatial from temporal cusp structures, at least two satellites are needed in the cusp simultaneously. Under this restriction, modeling of a cusp ion structure has been another way to study the relationship between cusp ion structures and reconnection. *Onsager et al.* [1995] developed a model of a cusp ion structure that traces ionospheric particles back to the magnetopause along their guiding center with the electromagnetic field configuration obtained from the *Stern* [1985] magnetic field model and simple dawn-dusk electric fields. They reconstructed spatial structures observed by two different Dynamics Explorer satellites, suggesting the existence of steady reconnection at the dayside magnetopause. *Wing et al.* [2001] improved Onsager's model by using magnetic fields from the T96 model [*Tsyganenko and Stern*, 1996] and electric fields from statistical APL convection patterns [*Ruohoniemi and Greenwald*, 1996]. *Wing et al.* [2001] predicted double dispersions during strong IMF B_y and weak negative B_z, and verified the prediction by comparison with observations by the DMSP satellites during similar IMF conditions. The models of *Onsager et al.* [1995] and *Wing et al.* [2001], however, use empirical field models which provide time-stationary electromagnetic fields, so their studies are limited to cusp structures during constant solar wind and IMF (SW-IMF) conditions.

[8] In this paper, we present a new model of cusp ion structures that is also valid for dynamic SW-IMF conditions. The model uses the Liouville theorem particle tracer (LTPT) together with the OpenGGCM three-dimensional global magnetosphere-ionosphere MHD model. The LTPT traces cusp ions back to the magnetosheath by integrating the Lorentz equation and the equation of motion. Then it calculates the phase-space densities of the cusp ions on the basis of their velocity information and the velocity distribution in the magnetosheath, employing Liouville's theorem. While the forward tracing method, also called large-scale kinetics (LSK) [*Peroomian*, 1994; *Peroomian et al.*, 2006], needs to launch numerous ions from the upstream region to gather enough ions in the cusp, the backward tracing of the LTPT traces only ions precipitating into the cusp and therefore avoids unnecessary calculations. The OpenGGCM solves resistive MHD equations with SW-IMF input from ACE or Wind, and provides time-dependent electromagnetic fields for the LTPT as well as number density, velocity, and plasma pressure. A major difference in our model from the previous models is that the ions move freely in 3D space by interacting with time-dependent electromagnetic fields under various SW-IMF conditions. We verify our model's validity by reproducing the cusp ion structures observed from three cusp-crossing events of Cluster and Polar satellites. We also demonstrate our model's utility to distinguish whether the cusp ion structures are temporal or spatial by studying the magnetopause movement and the trajectories of precipitating ions.

[9] In section 2, we introduce the model used in this study. In section 3, we present the results from three different case studies. We compare the model results with the observations and investigate their temporal versus spatial nature. In section 4, we summarize our results.

2. Modeling Method

[10] We use two models to construct a cusp ion structure, the OpenGGCM 3D global magnetosphere-ionosphere MHD model and the Liouville theorem particle tracer (LTPT). The OpenGGCM model solves resistive MHD equations in stretched Cartesian grids with SW-IMF input from ACE or Wind and provides number density, velocity, plasma pressure, and electromagnetic field. In this study, we set the OpenGGCM's simulation box at [x = −300–24 R_E, y = −48–48 R_E, z = −48–48 R_E] in GSE coordinates. A total of 36 M grid cells are used and they are most densely located in the dayside magnetosphere, in order to obtain high-resolution in this region. The time resolution of the OpenGGCM output fields that are used by LTPT models is 1 min.

[11] Since the OpenGGCM model used in this paper does not include the dynamic process of the plasmasphere and the ring current, we gradually replace the MHD electromagnetic field with the dipole magnetic field and the corotational electric field in the region between 7 and 5 R_E. Thus, the magnetic (electric) field used to integrate particle trajectories in the LTPT model is a pure dipole field (a pure corotational electric field) inside of 5 R_E, purely the MHD magnetic

(electric) field outside of 7 R_E, and in between, a linear combination of the two magnetic (electric) fields.

[12] The cusp in the OpenGGCM tends to be located at a lower latitude than in reality, while the empirical models of Onsager and Wing have the cusp at the right position by using the empirical magnetic field models such as T96 [*Tsyganenko and Stern*, 1996]. This may be because the OpenGGCM produces excessive plasma flow into the cusp or because a weak ring current in the OpenGGCM moves the magnetopause earthward, locating the cusp at a lower latitude. The exact location of the cusp, however, does not matter much for the purpose of this study since the precipitation signatures as shown later in this paper are not very sensitive to the exact geometry of the spacecraft crossing. To obtain the right cusp ion structures for our case studies, we shift the satellite orbits toward the modeled cusp. More detailed information about the OpenGGCM model is given by *Raeder* [2003] and *Raeder et al.* [1998, 2001].

[13] The LTPT is divided into two components: an ion tracer and a density calculator. The ion tracer tracks cusp ions back to the magnetosheath. It calculates the position and velocity of the ions by integrating the Lorentz equation and the equation of motion using the fourth-order Runge–Kutta method with a time step of 0.05 times the local gyroperiod. The electromagnetic fields necessary for the tracer are obtained from the OpenGGCM. Since the OpenGGCM provides the electromagnetic fields at its grids and at every minute, we use a linear interpolation in space and time to get the fields at a given position and at a given time.

[14] The ion tracer launches 336 cusp ions per minute along a satellite orbit. These ions have 28 logarithmically distributed energies from 25 eV to 32 keV, and 12 equally distributed pitch angles from 7.5° to 172.5°. The energy and pitch angle bins are same as the ones used in the Toroidal Imaging Mass-Angle Spectrograph (TIMAS) on Polar [*Shelley et al.*, 1995], and are chosen in order to compare our result with Polar observation. The same energy and pitch angle bins are also used for modeling Cluster observations, since the Cluster Ion Spectrometries (CIS) on Cluster satellites [*Rème et al.*, 2001], which have 31 energy bins between 5 eV to 35 keV and 8 pitch angle bins between 11.25° and 168.75°, observe similar energy and pitch angle ranges as TIMAS on Polar. The ion tracer introduces particles at only one arbitrary phase angle since the phase-angle does not have significant impact on the ion trajectory because of gyromotion, which has been tested with our model.

[15] The tracer stops its backward tracing when the cusp ion reaches the simulation box of the ion tracer [x = −50–20 R_E, y = −45–45 R_E, z = −45–45 R_E], when it reaches an altitude of 300 km, or when it travels 200 R_E. We set the 200 R_E limit to avoid calculation of magnetospheric ions which undergo bounce and drift motion. In this paper, we trace the cusp ions for 1–2 h until our model uses all the time series of the OpenGGCM fields. Because of this time limit, our model tends to show a small number of low-energy ions, especially at high latitudes. The ions precipitating at high latitudes usually originate from the nightside magnetopause, as shown in Figure 3a of *Wing et al.* [2001]. Since the nightside magnetopause is farther from the cusp than the dayside magnetopause, 1–2 h may not be enough for the low-energy ions to reach the tailward magnetopause. Therefore, our model does not produce a good spectrogram at the low-energy level. However, our model produces high-energy part reasonably well and the observers often focus on this part to study the relation between cusp structures and dayside reconnection. The lack of low-energy ions in a modeled spectrogram can be solved by running the OpenGGCM for a longer period.

[16] The density calculator in the LTPT searches the cusp ions coming from the magnetosheath and calculate their phase-space densities (PSDs). First, we determine a magnetosheath plane by calculating the magnetopause location. We fit the magnetopause to a paraboloid to points of maximum number-density gradients along the x axis at y = z = 0 R_E and along the y and z axes on the yz plane at x = 5, 0, −5, −10, −20, −30 R_E. We calculate the magnetopause every minute during the satellite's cusp-crossing event and select the magnetopause model with the largest standoff distance as the magnetosheath plane. We consider a cusp ion as coming from the magnetosheath if it reaches the selected magnetosheath plane. While the empirical models of *Onsager et al.* [1995] and *Wing et al.* [2001] have another step to calculate energy gain or loss across the magnetopause, the ion tracer of LTPT handles the process internally in the OpenGGCM which provides magnetopause properties, such as the magnetic field shear and the magnetopause current.

[17] Then, we calculate PSDs of the magnetosheath ions by using their velocities in the magnetosheath and the velocity distribution of the magnetosheath. The velocity distribution is calculated under the assumption that the magnetosheath ions can be represented by a kappa distribution:

$$f(\mathbf{r},\mathbf{v},t) = \frac{n(\mathbf{r},t)}{\pi^{3/2} w_0^3 \kappa^{3/2}} \frac{\Gamma(\kappa+1)}{\Gamma(\kappa-1/2)} \left(1 + \frac{|\mathbf{v}-\mathbf{v_d}(\mathbf{r},t)|^2}{\kappa w_0^2}\right)$$

$$w_0 = \sqrt{\frac{2kT}{m}} \left(\frac{\Gamma(\kappa-1/2)}{\kappa\Gamma(\kappa-3/2)}\right)^{1/2},$$

where n, v_d, and T are the number density, drift velocity, and plasma temperature, obtained from the OpenGGCM, respectively, and w_0 is the most probable speed. In this paper, we use κ = 7 on the basis of the work by *Wing et al.* [2001]. According to Liouville's theorem, the phase-space density in a collisionless system is conserved along a particle trajectory. Since the reconnection diffusion region is very small, we assume that all ions behave as they would be in a collisionless system. Therefore, the PSD calculated in the magnetosheath is the same as the one observed in the cusp.

[18] Finally, we calculate differential flux or energy flux by using the PSDs and display the flux as an energy-time spectrogram. As we calculate the differential flux based on velocity distribution of the magnetosheath plasma, the model results may be affected by the distribution function as well as the simulated magnetosheath which provides density, velocity, and temperature for the source distribution function. We verified the robustness of our model results by introducing different kappa values including $\kappa = \infty$ which is the Gaussian distribution, and different magnetosheath planes which changes the magnetosheath parameters. In spite of these changes, the main features of cusp spectrograms remain the same.

[19] The modeled spectrogram, however, tends to have higher flux than the observations. The same overestimation

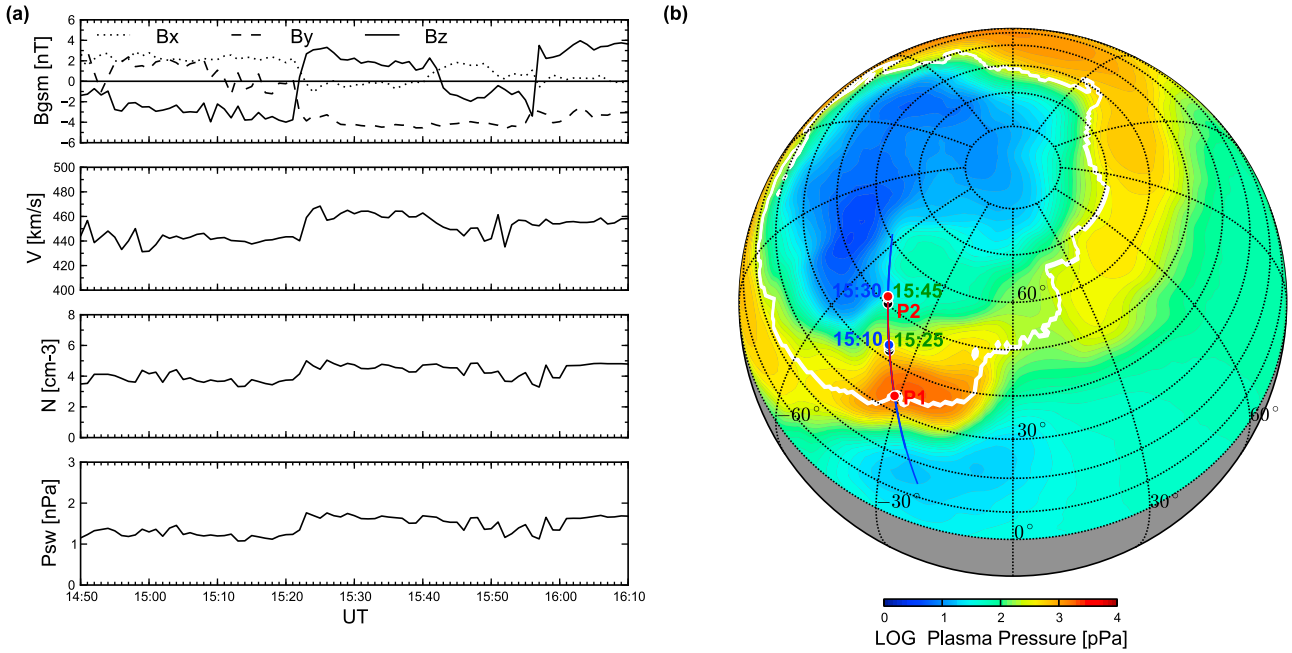

Figure 1. (a) Solar wind (SW) and interplanetary magnetic field (IMF) conditions obtained from ACE on 23 September 2004. IMF, velocity, number density, and dynamic pressure are plotted. In order to account for the SW-IMF propagation to the cusp, 10 min are added to the OMNI data. (b) The Cluster orbit (blue line) projected on the sphere of radius 5 R_E. The plasma pressure (color contour) and the open-closed field line boundary (white line) at 15:20 UT are calculated from the OpenGGCM simulation. C1, C3, and C4 are located between the black, green, and blue dots, respectively, during the event. The red line between P1 and P2 is an orbit used for modeling a cusp ion structure.

was found in the *Onsager et al.* [1995] model. Since only a part of the magnetosheath plasma is transmitted at the rotational discontinuity [*Cowley*, 1982; *Gosling et al.*, 1990; *Smith and Lockwood*, 1996], *Onsager et al.* [1995] introduce the reflection coefficient at the magnetopause to match the modeled results with the observations. Our model, however, assumes no collision throughout the particle's trajectory from the cusp to the magnetosheath, and therefore does include the reflection at the magnetopause. The higher fluxes in the model have likely other causes, for example, the lack of particle scattering by waves in the model.

[20] The LTPT model, therefore, acts like the TIMAS instrument onboard the virtual satellites. The ion tracer of the LTPT measures energy and pitch angle of the precipitating solar wind ions with a time resolution of a minute. The density calculator of the LTPT measures differential flux of these ions.

[21] In section 3, we test our model's validity by comparing the model results with the observations. We assess whether the model predictions are "excellent," "good," "satisfactory," or "unsatisfactory" according to the following four criteria: (1) dispersion in the correct direction is present, (2) distinct steps visible in the observations are also present in the predicted structures, (3) the slope of the upper edge of the dispersed structure agrees within a factor of 2, and (4) the highest energy of dispersed ions coincides to within a factor of 2. If all four criteria are fulfilled without ambiguity we call the fit excellent. If either three of the four criteria are fulfilled without ambiguity or all four are fulfilled, but with some ambiguity, we call the match good. If three of the four criteria are fulfilled with some ambiguity, we call the match satisfactory. Otherwise, the match is called unsatisfactory.

3. Model Results and Discussion

3.1. The 23 September 2004 Case

[22] The first case is a cusp-crossing event of Cluster on 23 September 2004. The Cluster satellites pass the northern cusp while southward IMF turns into northward IMF. This event was studied by *Escoubet et al.* [2008b] and we select this event to check our model's validity during the IMF change.

[23] Figure 1a shows the SW-IMF obtained from ACE. IMF B_z changes its sign around 15:22 UT. The number density, velocity, and solar wind pressure are about 4 cm^{-3}, 450 km/s, and 1.5 nPa. The OpenGGCM simulation is run with these SW-IMF conditions as input. Figure 1b shows Cluster orbits projected on a sphere of radius 5 R_E. The plasma pressure and the open-closed field line boundary at 15:20 UT are calculated from the OpenGGCM and projected on the same sphere of radius 5 R_E as the color contour and the white line, respectively. The blue line is the orbit of three Cluster satellites C1, C3, and C4. The locations between the blue and green dots with time labels show where and when C3 and C4 observe the cusp ion structures. Satellite C1 is 2 min behind satellite C4.

[24] The cusp is located near −30° GSE longitude where plasma pressure is very high (the red region in Figure 1b). As the Cluster satellites are located outside of the model cusp, we shift the orbits toward the OpenGGCM's cusp in

order to model cusp ion structures. Since the three Cluster satellites pass the same part of the cusp, we select only one orbit for modeling the three Cluster observations (the red line between two red dots, P1 and P2).

[25] In order to understand how a cusp structure changes in response to SW-IMF changes, we launch a total of 41 virtual satellites, one satellite every minute between 14:53 and 15:33 UT. We record the cusp ion structures for 40 min along the red line from P1 to P2. The speed of our virtual satellites are set at around 4.7 km/s, corresponding to the Cluster satellite speed. We present 15 of our results in Figure 2a for a quick look at the dependence of a cusp ion structure on the satellite crossing time. Each cusp structure is labeled with a satellite number. The satellites enter the cusp sequentially, and the low-numbered satellites enter the cusp earlier than the high-numbered satellites.

[26] The virtual satellites S01–S09 pass the cusp while southward IMF changes into northward IMF. Satellites S01–S04 observe normally dispersed structures in spite of the IMF change. This is because the magnetosphere is still influenced by the southward IMF. The S05–S09 virtual satellites begin observing the reverse dispersions at the end of the spectrograms. The S10–13 virtual satellites enter the cusp during northward IMF and observe irregularly dispersed structures. This irregularity may appear because the magnetosphere adjusts to the IMF change at this time. The normal dispersions shown at the beginning of the S09–S11 observations have weaker energy flux than the ones in the S05–S08 observations, indicating that the subsolar reconnection becomes weaker as IMF turns northward. The S14–S15 virtual satellites observe reverse dispersion of high-energy cutoff and this structure persists until the end of our model run.

[27] Figure 2b shows as a function of time the latitude along the Cluster orbit where the open-closed field line boundary (OCB) is located. The white area represents the open field line zone and the grey area represents the closed field line zone. The black line shows the OCB, and the red line shows the P1 location. We also show the magnetopause standoff distance (the blue line) by calculating the location of maximum current density along the Sun-Earth line.

[28] The OCB slowly moves to the higher latitudes since IMF changes northward, because the subsolar reconnection changes into the lobe reconnection. At 15:23 UT, we observe northward motion of OCB location together with earthward movement of the magnetopause. This may relate to the sudden increase of solar wind pressure at 15:23 UT since northward IMF usually expands the magnetopause. The increased pressure may shrink the magnetopause and compress the magnetosphere. Since the OCB in Figure 2b is calculated at the altitude of Cluster near 4 R_E, the OCB at this altitude moves to a higher latitude because of the compression. Then, the magnetosphere adjusts quickly to the new pressure and the closed field line is back to normal, therefore moving the OCB back to a lower latitude. Note that S03–S09 observe a bump around 15:23 UT in Figure 2a. They observe high-energy ions since the northward movement of OCB pushes newly opened field lines to the higher latitude.

[29] The comparison of our modeled results with Cluster observations are shown in Figure 2c. Figure 2c (left) shows the spectrograms observed from Cluster spacecraft C4, C1, and C3. Figure 2c (right) shows three selected spectrograms from the simulations. The V1 is the S02 in Figure 2a, the V2 is the virtual satellite launched between S02 and S03, and the V3 is the virtual satellite launched between S11 and S12. For the model-observation comparison, we fit the straight line, $\log E = aT + b$, where E is energy, T is time, a is the slope, and b is the intercept, to the upper edge of each dispersion by using the linear least squares. The magenta lines represent the upper edges and the white lines represent the fitted lines. In each spectrogram, we display the highest energy of the upper edge, i.e., the highest energy of the dispersed ions, and the slope a of the fitted line.

[30] The C4 and C1 probes pass the cusp during southward IMF, observing normally dispersed structures. The dispersion slopes in the C4 and C1 observations are $(-2.116 \pm 0.051) \times 10^{-3}$ and $(-2.128 \pm 0.029) \times 10^{-3}$, and the highest energies of the dispersed ions are about 27.61 and 28.90 keV. The V1 and V2 also observe normal dispersions, similar to the C4 and C1 observations. The dispersion, however, appears a few minutes earlier than the observations and the dispersion has a smaller slope. The model orbit may expose the virtual satellites to a slightly different environment than the Cluster satellites, causing these differences. The slopes of both modeled dispersions are $(-1.067 \pm 0.113) \times 10^{-3}$ and $(-1.040 \pm 0.133) \times 10^{-3}$. The highest energies of both dispersions are 32 keV.

[31] Our model successfully reproduces normal dispersions, the distinct structures of C4 and C1 observations. This fulfills the comparison criteria 1 and 2 which we stated in section 2. The difference between the modeled and observed dispersion slopes are about a factor of 2 within the error margin, satisfying the criterion 3. The highest energies of both modeled and observed dispersions also coincide within a factor of 2, satisfying criterion 4. Since both V1 and V2 spectrograms fulfill all four criteria, we consider that the model predictions are excellent.

[32] The C3 probe passes the cusp after the IMF turns northward and observes an irregular ion structure. The upper edge of this dispersion is flatter than the ones in the C1 and C3 observations. The beginning of this structure shows the widening of high-flux region with the decreasing low-energy edge and the increasing high-energy edge. The virtual satellite V3 also observes an irregularly dispersed structure with a flatter upper edge than the ones in the V1 and V2 observation. The widening high-flux region is also visible at the beginning of the V3 spectrogram. These patterns satisfy the comparison criteria 1 and 2.

[33] The slopes of both modeled and observed structures are $(-0.328 \pm 0.124) \times 10^{-3}$ and $(-0.221 \pm 0.044) \times 10^{-3}$, matching within a factor of 2 and thus satisfying criterion 3. The highest energy of the modeled dispersion, however, is 21.53 keV, more than 2 times higher than the highest energy of the observed dispersion, 9.24 keV. Therefore, the criterion 4 is not satisfied. As three of four criteria are fulfilled without ambiguity, the model result of the C3 observation is considered as being good.

[34] Note that the high-energy flux bands around 10 keV seen in the Cluster observations are not present in the model results. Since our model considers only ions that originate from the magnetosheath, it does not reproduce these bands, which are composed of hot magnetospheric ions.

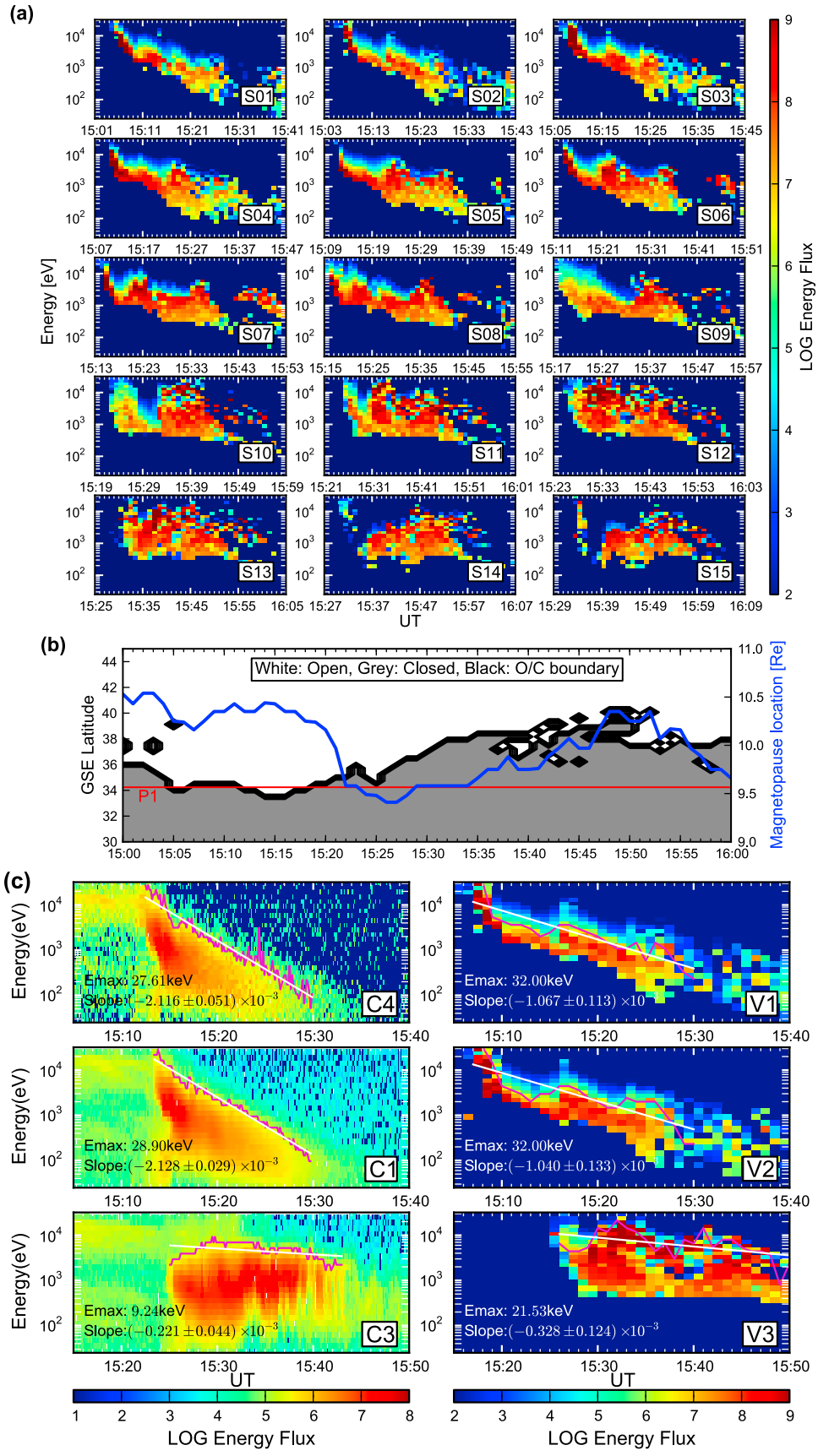
(a)
Energy [eV]
UT
LOG Energy Flux
S01
S02
S03
S04
S05
S06
S07
S08
S09
S10
S11
S12
S13
S14
S15
(b)
White: Open, Grey: Closed, Black: O/C boundary
GSE Latitude
Magnetopause location [Re]
P1
(c)
Energy(eV)
Emax: 27.61keV
Slope:(−2.116 ±0.051) ×10^−3
C4
Emax: 32.00keV
Slope:(−1.067 ±0.113) ×10^−3
V1
Emax: 28.90keV
Slope:(−2.128 ±0.029) ×10^−3
C1
Emax: 32.00keV
Slope:(−1.040 ±0.133) ×10^−3
V2
Emax: 9.24keV
Slope:(−0.221 ±0.044) ×10^−3
C3
Emax: 21.53keV
Slope:(−0.328 ±0.124) ×10^−3
V3
UT
LOG Energy Flux

Figure 2

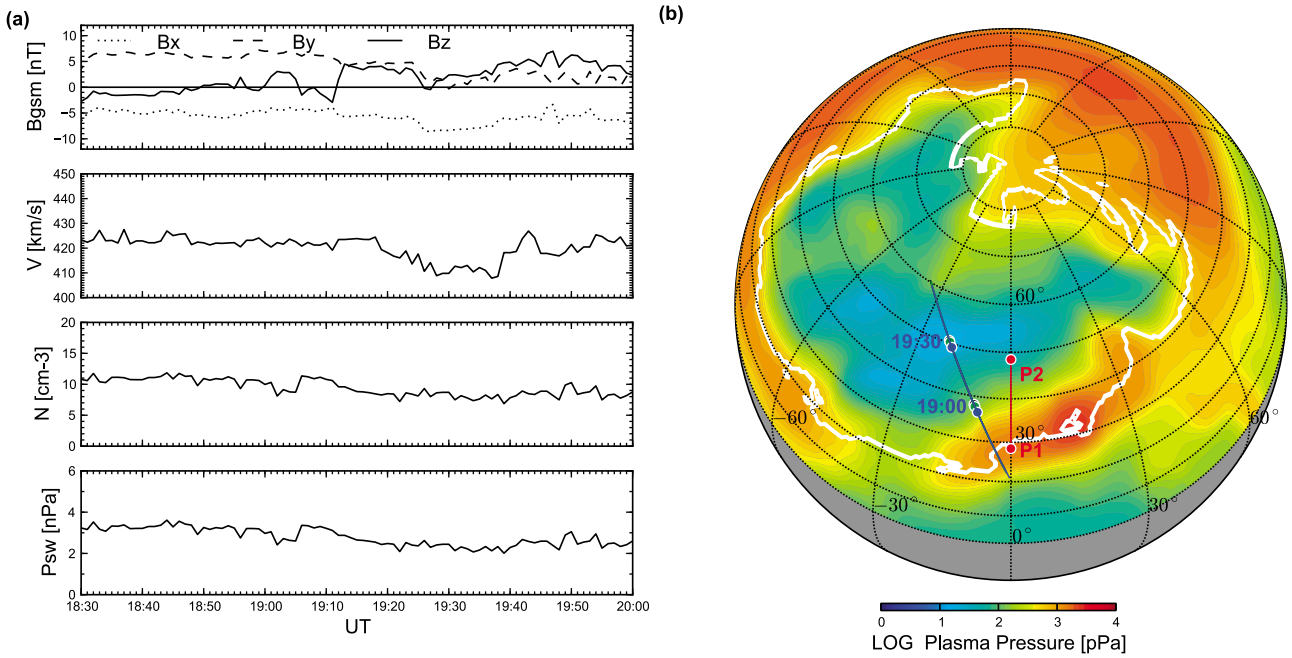

Figure 3. (a) Solar wind and IMF conditions obtained from ACE on 28 August 2003. To account for SW-IMF propagation from ACE to the cusp, 65 min are added to the ACE data. (b) The Cluster orbit (blue line) projected on a sphere of radius 5 R_E. Plasma pressure (color contour) and the open-closed field line boundary (white line) at 19:10 UT are calculated from the OpenGGCM simulation. Cluster C1, C3, and C4 are located between the black, green, and blue dots, respectively, during the event. The red line between P1 and P2 is the orbit used for modeling a cusp structure.

3.2. The 28 August 2003 Case

[35] The second case is a cusp-crossing event of Cluster on 28 August 2003. While SW-IMF conditions are quite variable, Cluster satellites (C1, C3, and C4) sequentially enter the cusp and observe slightly different dispersions. This event was introduced by *Escoubet et al.* [2008c], and we choose this event to prove our model's validity and study temporal variations of these cusp structures.

[36] The SW-IMF conditions obtained from ACE are shown in Figure 3a and are used as an input for the OpenGGCM. IMF B_z changes its sign several times during 18:55–19:15 UT while IMF B_x and B_y show little variation. Figure 3b shows the Cluster orbit (the blue line) projected on a sphere of radius 5 R_E. We calculate plasma pressure and the open-closed field line boundary at 19:10 UT with the OpenGGCM results and project them on the same sphere. Cluster satellites C1, C3, and C4 are located between the black, blue, and green dots while observing the ion dispersions. Since they do not pass the OpenGGCM's cusp, which is the high plasma pressure region, we shift the orbit (the red line from P1 to P2) to model the cusp structures.

[37] We launch a total of 15 satellites, one every minute between 18:55 and 19:10 UT along the red line, in order to find cusp structures similar to Cluster observations. Each satellite observes a cusp structure for 40 min. This approach is justified because there is considerable uncertainty in propagating the SW-IMF from the ACE observations ~226 R_E upstream of Earth and ~23 R_E off the Sun-Earth line to the inflow boundary of the simulation 24 R_E upstream of Earth. By launching one satellite every minute, we can also investigate how a cusp ion structure changes in time and find out if any of these modeled ion structures compare reasonably well with the observations.

[38] We present our results in Figure 4a. As in the previous case, low-numbered satellites pass the cusp earlier than high-numbered satellites. Double dispersion shown in the S01–S03 spectrograms becomes one thick dispersion with a flat high-energy cutoff around 19:05 UT in the S04–S05 spectrograms. S06–S08 also observe double dispersions, one at the beginning and another starting at ~19:16 UT. Then, S09–S15 observe continuously dispersed structures with irregular high-energy cutoff.

[39] To study the magnetosheath origins of cusp ions, we calculate where on the magnetosheath plane the ions penetrate. The magnetosheath plane is where we calculate PSDs. We project the ion entry points on the YZ plane as seen from the Sun in Figure5a. To relate the origins to cusp ion structures, we color the points according to the time observed by

Figure 2. (a) Model results of the Cluster event on 23 September 2004. (b) The open-closed field line boundary (black line) along the Cluster orbit and the magnetopause standoff distance (blue line). The red line represents the P1 location. (c) Comparison of the modeled results with Cluster observations. The magenta lines show the upper edges of dispersions, and the white lines show the fitted lines to the upper edges. The highest energy of dispersed ions and the slope of the fitted line are labeled in each spectrogram.

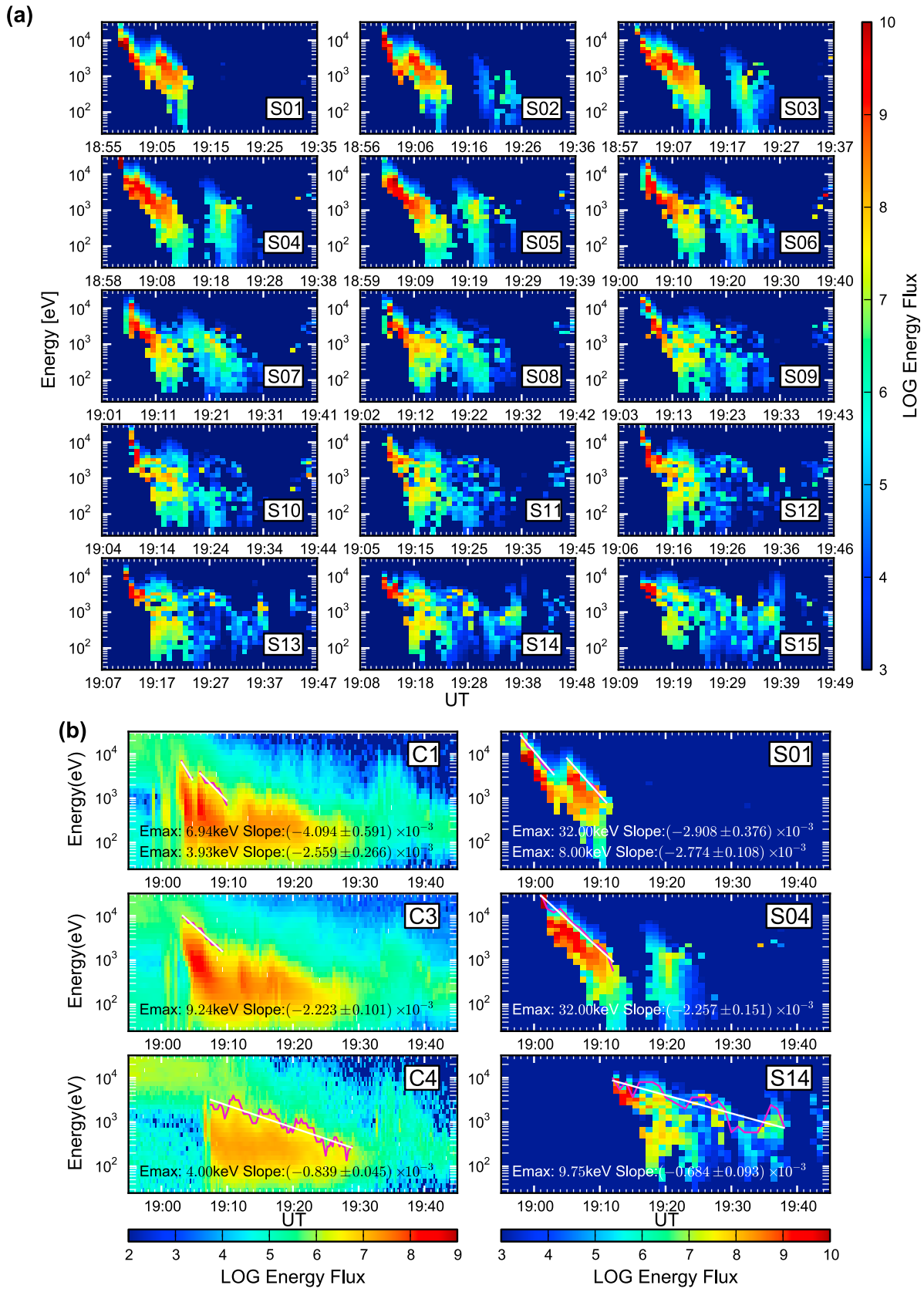

Figure 4. (a) Model results of the Cluster event on 28 August 2003. (b) Comparison of the modeled results with Cluster observations. The magenta and white lines are the upper edges of dispersions and the fitted lines to the upper edges, respectively. The highest energies of dispersions and the slopes of the fitted lines are also displayed.

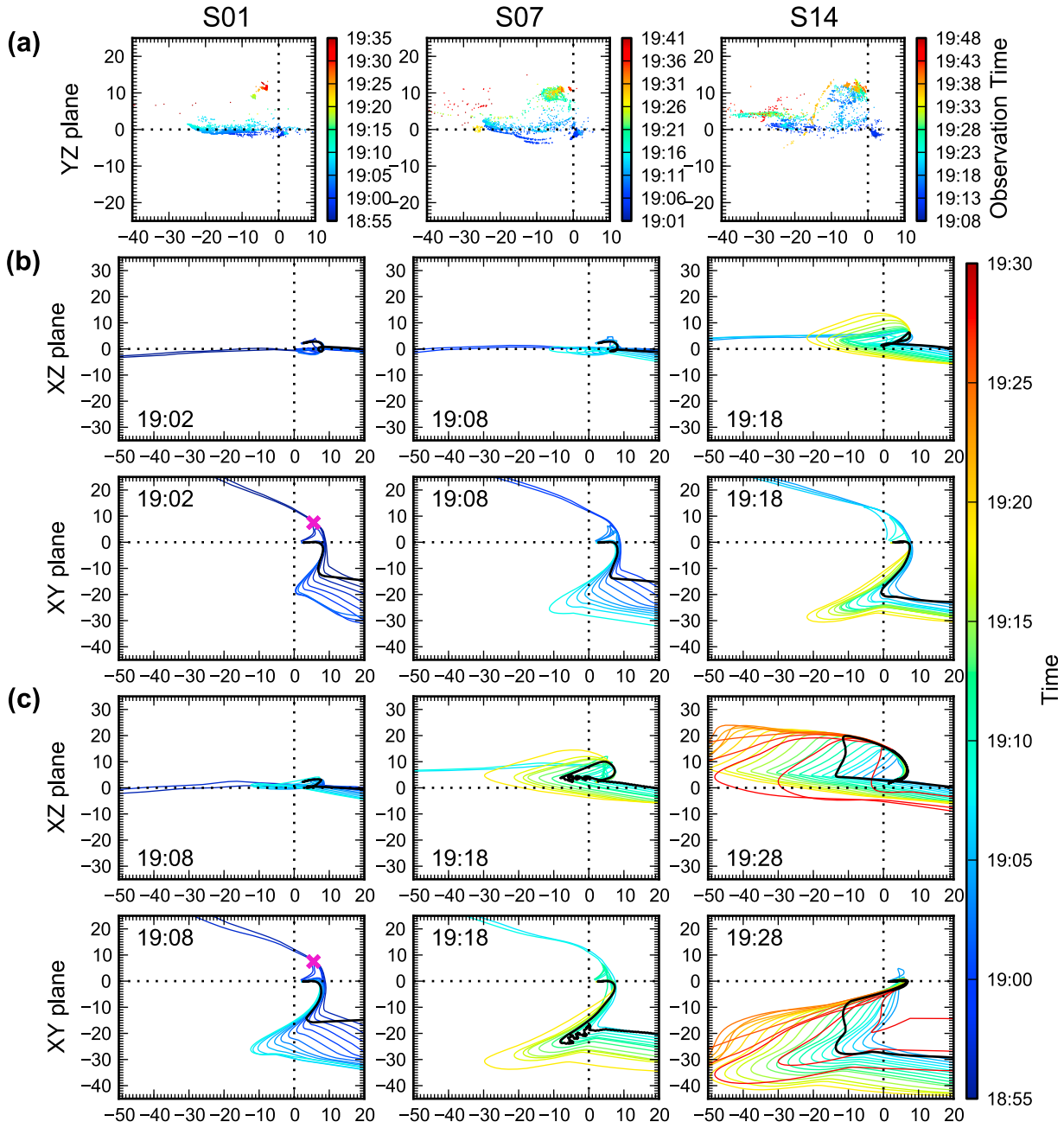

Figure 5. (a) Ion entry points on the magnetosheath plane, projected on the YZ plane as viewed from the Sun. The first, second, and third columns show the S01, S07, and S14 observations, respectively. The color represents the time when the satellites observe the ions. The magenta crosses represent the reconnection site shown in Figure 6a. (b, c) Two ion trajectories (black lines) observed by each satellite, projected on the XZ and XY planes. The colored lines are magnetic field lines calculated every minute along the ion trajectories. The indicated time represents when the ion is observed by a satellite.

the satellites. The first, second, and third columns of Figure 5a show the entry points of ions observed by S01, S07, and S14, respectively. Then, we trace the ions into the magnetosphere until they reach the point where they are observed. We select two example ions and trace the magnetic field lines on which each ion has been. Figures 5b and 5c show the two ion trajectories (black lines) and the magnetic field lines (colored lines) calculated every minute along the trajectories. The color shows the time when each ion is on each field line.

[40] The ions observed by S01 come mostly from the dawnside of magnetosheath along Zgse = 0 axis. Especially, the ions observed before 19:05 UT, which compose the first dispersion of S01, have the same magnetosheath origin as the ions observed during 19:05–19:10 UT, which compose the second dispersion of S01. We select two ions, one from

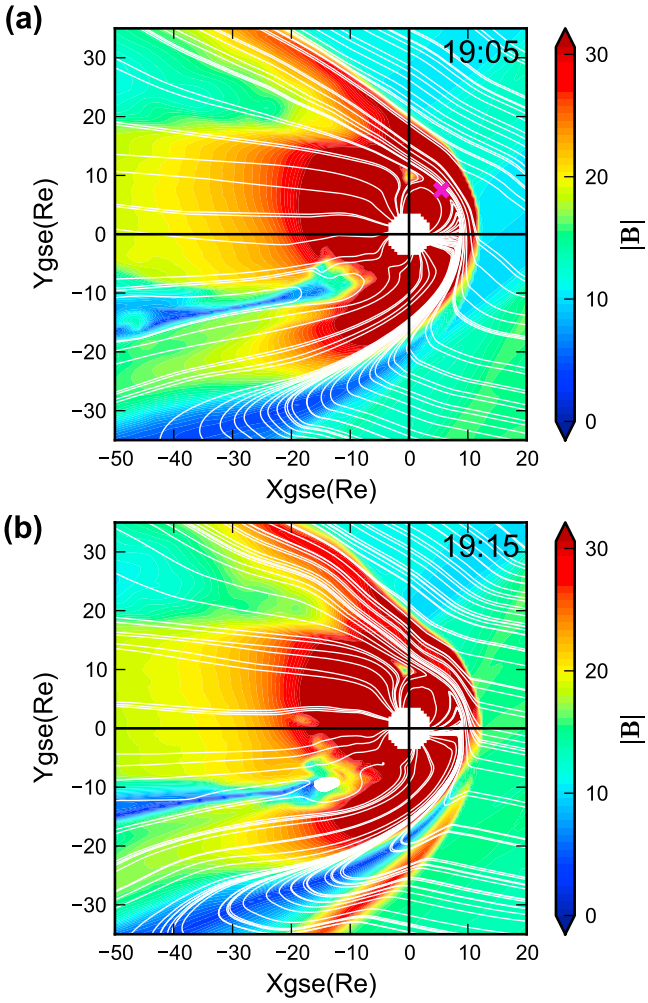

Figure 6. Magnetic configuration of the GSE equatorial plane (a) at 19:05 UT and (b) at 19:15 UT. The color contour represents the magnitude of magnetic field, and the magenta cross in Figure 6a represents the reconnection site on the duskside magnetopause.

each dispersion, and show the trajectories in the first column of Figures 5b and 5c. Although the ions arrive at S01 at different times, both of them pass the similar open field lines caused by reconnection on the duskside of magnetopause (the magenta crosses). The reconnection site is selected from Figure 6a where the magnetic configuration of the GSE equatorial plane at 19:05 UT is displayed on the contour of magnetic field magnitude. The reconnection appears on the duskside magnetopause where the dawnward IMF meets the duskward magnetospheric field. Since the ion precipitation originates from the same reconnection site at different times, this indicates that the double dispersions are temporal structures caused by variations of the reconnection rate on the duskside magnetopause.

[41] The second column of Figure 5a shows that the ions observed by S07 have two major regions of origin on the magnetosheath plane. The ions observed before 19:16 UT, which compose the first dispersion, are mostly from the dawnside magnetosheath along the Zgse = 0 axis while the ions observed after 19:16 UT, which compose the second dispersion, are from the dawnside northern magnetosheath near Zgse = 10. Two ion trajectories from each dispersion are shown in the second column of Figures 5b and 5c. The ion observed at 19:08 UT passes similar open field lines as the ions of S01, indicating that the first dispersion of S07 is caused by reconnection on the duskside magnetopause. The ion observed at 19:18 UT, however, precipitates to the cusp after traveling in a zigzag motion in the dawn flank of magnetosheath.

[42] This zigzag motion is the result of magnetic mirror force. Figure 6b shows magnetic configuration of the equatorial plane at 19:15 UT where the magnetic field magnitude is color contoured. We observe an increase of magnetic field at the sunward boundary of the dawnside magnetosheath as well as the strong magnetic field at the earthward boundary. Thus, the dawnside magnetosheath is surrounded by the regions of strong magnetic field. Since the magnetic mirror force repels a particle from a strong magnetic field region, the ion observed at 19:18 UT moves back and forth between the two boundaries. This ion eventually precipitates into the cusp as it moves closer to the nightside of the earthward boundary. The mirror force of this region is no longer strong enough to repel the ion because of the Earth's weak magnetic field. Therefore, the second dispersion of S07 is composed of ions temporarily trapped in the dawnside magnetosheath while the sunward boundary has a strong magnetic field. The enhanced field is caused by the reformation of the bow shock as the IMF rotates at 19:10 UT (see Figure 3a) from an orientation that creates a parallel shock on the dawnside to an orientation that produces a quasi-perpendicular shock. The interaction of the IMF rotation (either a rotational or a tangential discontinuity) with the bow shock apparently creates the transient magnetic cavity in the sheath. However, a detailed analysis of the mechanism responsible for the appearance of this strong magnetic field is beyond the scope of this paper.

[43] The ions observed by S14 have various source regions on the magnetosheath, shown in the third column of Figure 5a. They originate mostly from the dawnside flank of the magnetosheath near Zgse = 0 and Zgse = 5 and from the dawnside of northern lobe near Zgse = 10. We select two ions observed at two different latitudes by S14 to show the different path each ion takes depending on the latitude. The third column of Figures 5b and 5c shows trajectories of the two ions observed at 19:18 and 19:28 UT. Since S14 moves from low to high latitude, the ion observed at 19:28 UT precipitates at higher latitude than the one observed at 19:18 UT.

[44] The ion arriving at high latitudes originates from the nightside of the dawn flank magnetopause while the ion arriving at low latitude originates from the dayside of the magnetopause. The field lines on the nightside of dawn magnetopause are draped over the northern magnetopause and connected to high latitudes of the cusp by the reconnection on the duskside magnetopause. Therefore, the ion observed at the high latitude takes a longer way to arrive at the cusp from the magnetosheath, and 1–2 h of tracing time are not enough for these ions, especially low-energy ions, to travel between the magnetosheath and cusp. This is why the modeled spectrogram has weak or no energy flux at the low-energy level near the high latitudes.

[45] Figure 4b compares our model results to the Cluster observations. Figure 4b (left) shows the spectrograms observed

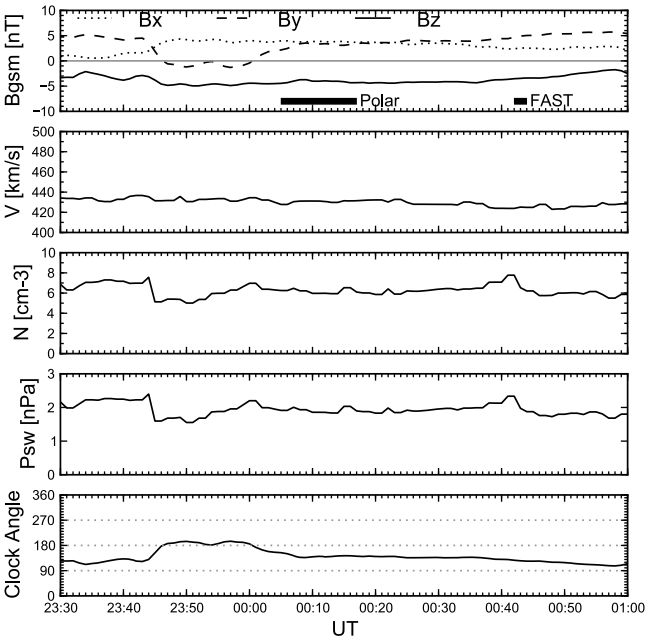

Figure 7. Solar wind and IMF conditions obtained from the Wind spacecraft on 25 August 1998. Horizontal bars in the first panel represent the time when FAST and Polar pass the low-latitude cusp. To account for the propagation from Wind to the magnetopause, 27 min are added to the Wind data.

from Cluster spacecraft C1, C3, and C4. Figure 4b (right) shows the modeled spectrograms observed from our virtual satellites S01, S04, and S14. As in Figure 2c, the magenta lines represent the upper edges of dispersions and the white lines are the fitted lines to the upper edges. We also present the slopes of the fitted lines and the highest energies of the dispersed ions in the spectrograms.

[46] S01 observes double dispersions while S04 observes one broad single dispersion. These patterns match with the C1 and C3 observations. Our results in Figure 5 suggest that the double dispersions are temporal structures caused by various reconnection rates on the duskside flank of magnetopause. Thus, the single thick dispersion shown in the C3 spectrogram may appear since C3 observes the second dispersion, caused by increased reconnection rate, right after observing the first dispersion at the entry into the cusp. The dispersion direction in the modeled spectrograms agrees with the one in the observations, fulfilling the comparison criterion 1. Our model, however, does not produce the flux at the low energy as seen in the observations because of the limited tracing time. Therefore, we consider that the model predictions fulfill the criterion 2 with some ambiguity.

[47] The slopes of the modeled double dispersions are $(-2.908 \pm 0.376) \times 10^{-3}$ and $(-2.774 \pm 0.108) \times 10^{-3}$, coinciding to the slopes of the observed double dispersions $(-4.094 \pm 0.591) \times 10^{-3}$ and $(-2.559 \pm 0.266) \times 10^{-3}$ within a factor of 2. The slopes of the modeled and observed single dispersions are $(-0.684 \pm 0.093) \times 10^{-3}$ and $(-0.839 \pm 0.045) \times 10^{-3}$, also matching within a factor of 2. Therefore, the S01 and S04 spectrograms fulfill the criterion 3. The highest energies of the double dispersions are 32.0 and 8.0 keV for the model and 6.94 and 3.93 keV for the observation. The highest energies of the single dispersions are 32.0 keV for the model and 9.24 keV for the observation. All the highest energies of the modeled dispersions are more than 2 times higher than the ones of the observed dispersions, thus failing the criterion 4. Since the model predictions on the C1 and C3 observations fulfill only three criteria with some ambiguity, the model results are considered as being satisfactory.

[48] Figure 4b (bottom) shows the observations of C4 and S14. S14 observes continuous normal dispersion with a wavy high-energy cutoff similar to the one that C4 observes. Therefore, the model prediction fulfills the comparison criteria 1 and 2. The wavy cutoff may be a result of fast convection speed of open field lines during intermittent reconnection on the duskside magnetopause. Thus, S14 observes a slight increase of high-energy cutoffs when S14 is connected to the newer open field lines, which have more ions of high energy. The OpenGGCM may not produce the intermittent reconnection at the same time as in reality, and therefore S14 observes the increase of high-energy cutoff at different times than C4.

[49] The dispersion slopes in the S14 and C4 spectrograms are $(-0.684 \pm 0.093) \times 10^{-3}$ and $(-0.839 \pm 0.0045) \times 10^{-3}$, satisfying the criterion 3. However, the highest energy of the modeled and observed dispersions are 9.75 and 4.0 keV, and therefore fails the criterion 4. Since three of all four criteria are fulfilled without ambiguity, the model result of S14 is considered as being good.

3.3. The 25 August 1998 Case

[50] The third case is a cusp-crossing event by Polar and FAST on 25 August 1998. Polar and FAST cross the northern cusp during stable solar wind conditions, and observe similar stepped dispersions although they enter the cusp at different times separated by 27 min. *Trattner et al.* [2002] concluded that the stepped structure is a spatial structure, caused by the spatial variation of reconnection. Here, we reproduce the cusp structure observed by Polar with our model and investigate whether it is spatial or temporal.

[51] Figure 7 shows SW-IMF conditions obtained from Wind. The black bars in the first panel represent the time when Polar and FAST reside in the low-latitude cusp. Both satellites pass the cusp during southward and duskward IMF. Figure 8 shows the Polar location (the blue lines) projected on spheres of radius 5 R_E. The color contours and white lines represent plasma pressures and open-closed field line boundaries at 00:15 and 00:25 UT, calculated from the OpenGGCM simulation.

[52] The OpenGGCM cusp, the region of high plasma pressure, is located in the vicinity of local noon at 00:15 UT, and moves to the duskside around 15° GSE longitude, which is near 13 MLT, at 00:25 UT. Then, the cusp stays on the duskside until 01:00 UT. Note that Polar and FAST observed the stepped dispersion at two different magnetic local times, 13:43 MLT and 14:57 MLT. This finding may relate to the cusp motion. Since Polar does not pass through the modeled cusp, we introduce two orbits, O1 and O2, which interact with the cusp centers at 00:15 and 00:25 UT. The O1 and O2 pass along the noon-midnight meridian and a longitudinal line at 15° GSE longitude which passes ~13 MLT. The altitudes of both orbits are 4 R_E, i.e., the Polar altitude.

[53] A total of five virtual satellites are introduced: one for comparison with the Polar observation, and the rest for

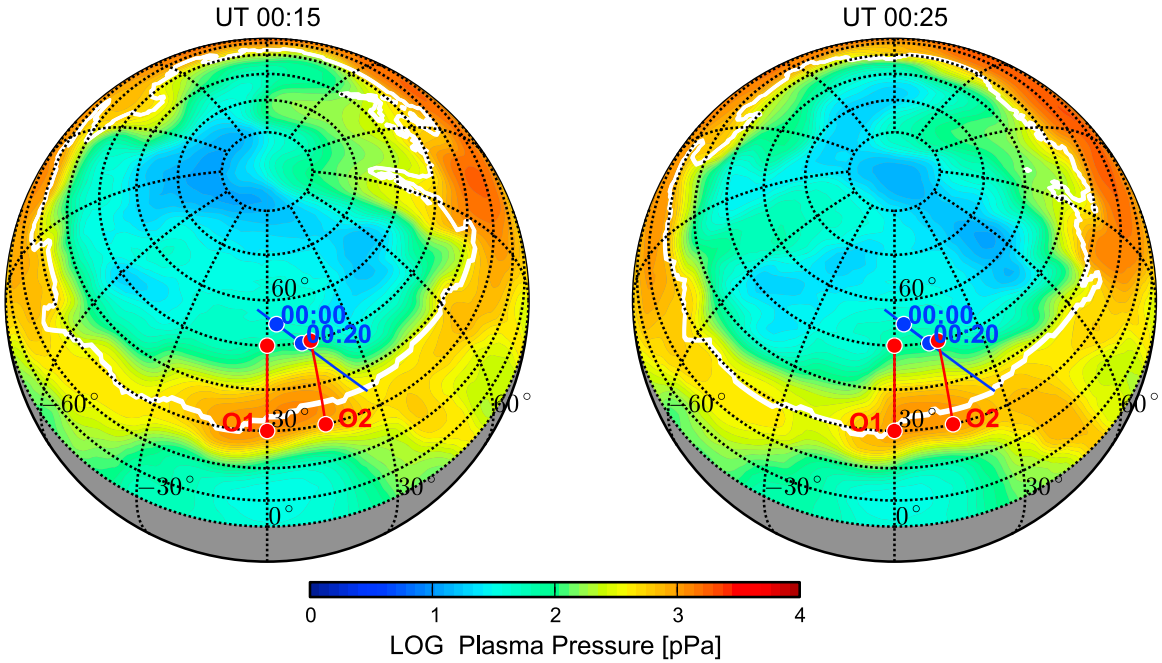

Figure 8. Polar orbit (blue line) projected on the spheres of radius 5 R_E. The plasma pressures (color contour) and the open-closed field line boundaries (white line) at 00:15 and 00:25 UT are obtained from the OpenGGCM simulation. Polar is located between the blue dots during the event. Red lines O1 and O2 are the orbits for our virtual satellites.

investigating whether the dispersed ion structure is of spatial or temporal nature. The first satellite (S1) passes the cusp along the O1 orbit during 00:20–00:05 UT. Since the cusp during this time is located near the local noon, we introduce O1 as S1's orbit. The speed of S1 is set at around 4 km/s, corresponding to the Polar speed. To increase the resolution of the spectrogram, we launch the ions every 30 seconds in this case. The spectrogram obtained from the S1 orbit is used to compare with the Polar observation in order to assess our model's validity.

[54] The remaining satellites (S2–S5) pass the cusp at 00:15, 00:25, 00:35, and 00:45 UT with infinite speed. Thus, these satellites provide spatial snapshots at these times, removing all temporal variations. Since the cusp center moves from noon to dusk around 00:20 UT, we select O1 as S2's orbit and O2 as the orbits of S3–S5. Note that FAST observed the stepped structure during 00:42–00:44 UT, 27 min after Polar observed the similar structure. If the structure is purely spatial, our virtual satellites S2–S5 should observe essentially the same cusp ion structures as S1 during 00:15–00:45 UT.

[55] Figure 9 shows the comparison between the Polar observation and the model results (S1–S5). The three vertical lines separate three steps in the cusp ion structures. We display the structures backward in time, i.e., increasing in latitude, as they were displayed in Figure 9 of *Trattner et al.* [2002]. The first two spectrograms on the left side are observed from Polar and S1 satellites and used for the model-observation comparison. The magenta and white lines represent the upper edges of the dispersions and the lines fitted to the upper edges. The highest energies of the dispersed ions and the slopes of the fitted lines are also presented.

[56] Although the orbit O1 is quite different from the Polar orbit, S1 observes continuously dispersed structures with high-energy ion injection in the first step, a wide high-flux region in the second step, and a rather flat dispersion in the third step. This result matches well with the Polar observation, and thus fulfills the comparison criteria 1 and 2. The slopes of observed and modeled dispersions agree within a factor of 2, satisfying the criterion 3. The highest energies of both dispersed ions, however, do not coincide within a factor of 2, failing the criterion 4. By fulfilling three criteria without ambiguity, the model prediction is considered as being good.

[57] The remaining spectrograms are used for analyzing whether the stepped dispersion is temporal or spatial. The spectrogram of S2, which is the cusp snapshot at 00:15 UT, shows very similar stepped structures as S1. After the cusp moves to dusk, S3–S5 pass the cusp at 00:25, 00:35, and 00:45 UT. Although their cusp structures are not quite same as the one in the S1 observation, the key properties of each step are still observed. The energy of cusp ions continuously decreases through the whole stepped structure as the latitude increases, and the second step has wider high-flux region than the first step. This stepped structure remains steady for 30 min between 00:15–00:45 UT, supporting the conclusion of *Trattner et al.* [2002] that the stepped dispersion is spatial.

[58] Figure 10, however, suggests that the stepped dispersion is not only spatial but has also temporal elements. We examine the magnetosheath origins of cusp ions by calculating ion entry points on the magnetosheath plane which is located a few tenths of a R_E outside of the magnetopause and where we calculated the PSDs. Figure 10a shows the projection of these points on the YZ plane as seen from the Sun. The entry points in Figure 10a (top) are

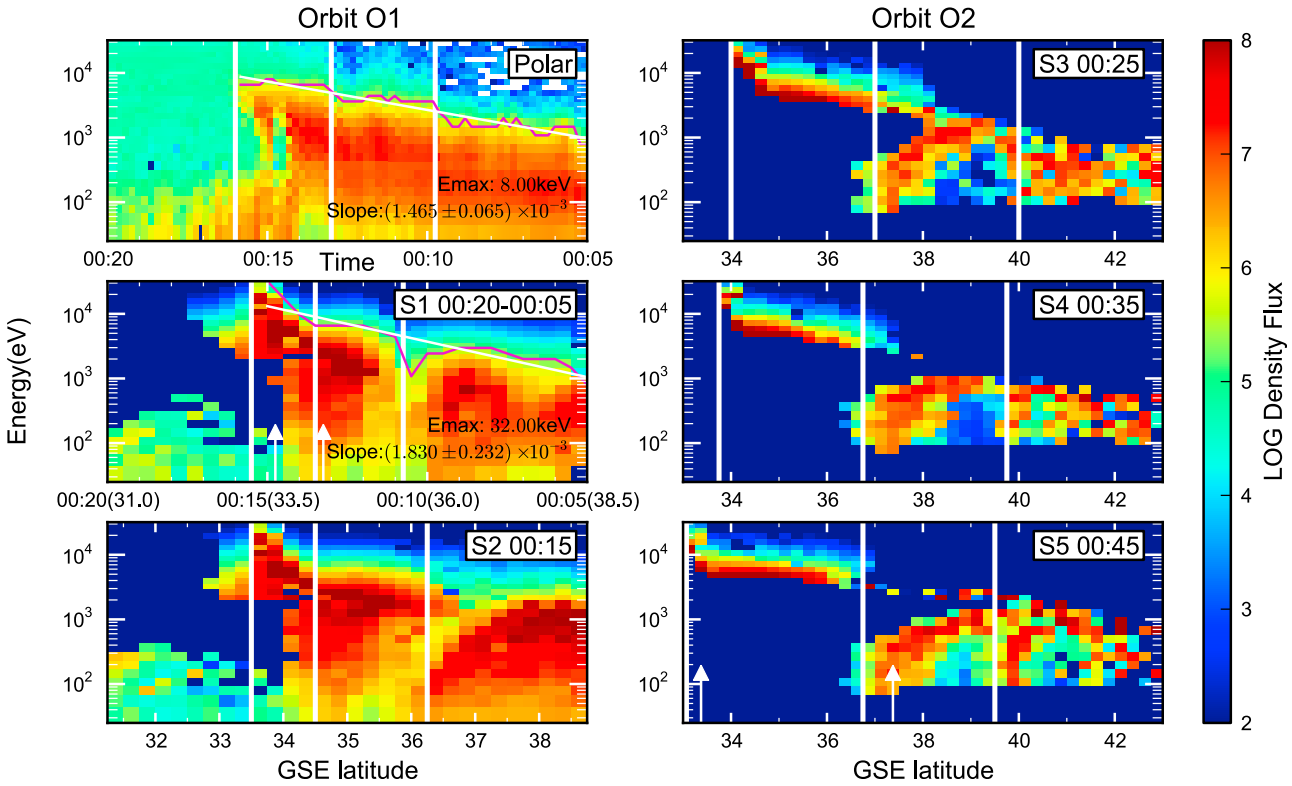

Figure 9. Comparison of the modeled results with Polar observation on 25 August 1998. The time next to the satellite number represents the time when the satellite passes the cusp. The white bars separate the three distinct structures, and the white arrows represent the selected positions for the ion trajectories in Figure 10b. The magenta and white lines in the Polar and S01 spectrograms represent the upper edges of dispersions and the fitted lines to the edges, respectively. The highest energies of dispersions and the slopes of the fitted lines are also displayed in the two spectrograms.

colored according to the latitude where the ions are observed in order to relate the points with the stepped dispersion. The entry points in Figures 10a (middle) and 10a (bottom) are colored according to the ion energy at the cusp and the time when the ions penetrate the magnetosheath plane in order to distinguish the magnetosheath source regions.

[59] Two magnetosheath source regions are mainly observed and easily distinguishable by the colors of entry points in Figures 10a (middle) and 10a (bottom). We point to the source regions with the magenta arrows in Figure 10a. One source region is located on the dawnside magnetosheath and moves toward local noon as the satellite orbit changes from O1 to O2 in order to pass the cusp center. Another source region is located on the duskside magnetosheath, and moves to the further duskside of the magnetosheath as the orbit changes. The ions from the dawnside source region are high-energy ions and precipitate mostly at the low and middle latitudes of the cusp, where the first and second steps are observed. The ions from the duskside source region are low-energy ions and precipitate at the middle and high latitudes of the cusp where the second and third steps are observed.

[60] The ion entry times on the magnetosheath plane are also different depending on the source regions. While the ions from the duskside source region enter the magnetosheath plane mostly before 00:10 UT, the ions from the dawnside source region have different entry times according to the satellites, i.e., about 00:10, 00:13, 00:22, 00:33, and 00:43 UT for S1–S5. Thus, there are two reconnection sites that produce these ions. The first site is located on the duskside magnetopause and disappears around 00:10 UT. The next site is located on the dawnside magnetopause near the local noon, and constantly active after 00:10 UT.

[61] To study how the ions from two different source regions penetrate the magnetopause, we select two typical ions, one from each source, and show their trajectories with magnetic field lines which they have passed. For simplicity, we display the results from only two satellites, S1 and S5, in Figure 10b. Figure 10b (top) shows the trajectories of ions from the dawnside source region, and Figure 10b (bottom) shows the trajectories of ions from the duskside source region. The black lines are the trajectories projected on XZ and YZ planes. The colored lines are the magnetic field lines, and the color represents the time when each ion is on each of the field lines. Each plot is labeled with the satellite number and the observed latitude.

[62] All ions from both source regions enter the magnetopause via kinked open field lines caused by subsolar reconnection. However, their trajectories are aligned with different IMF clock angles depending on the magnetosheath

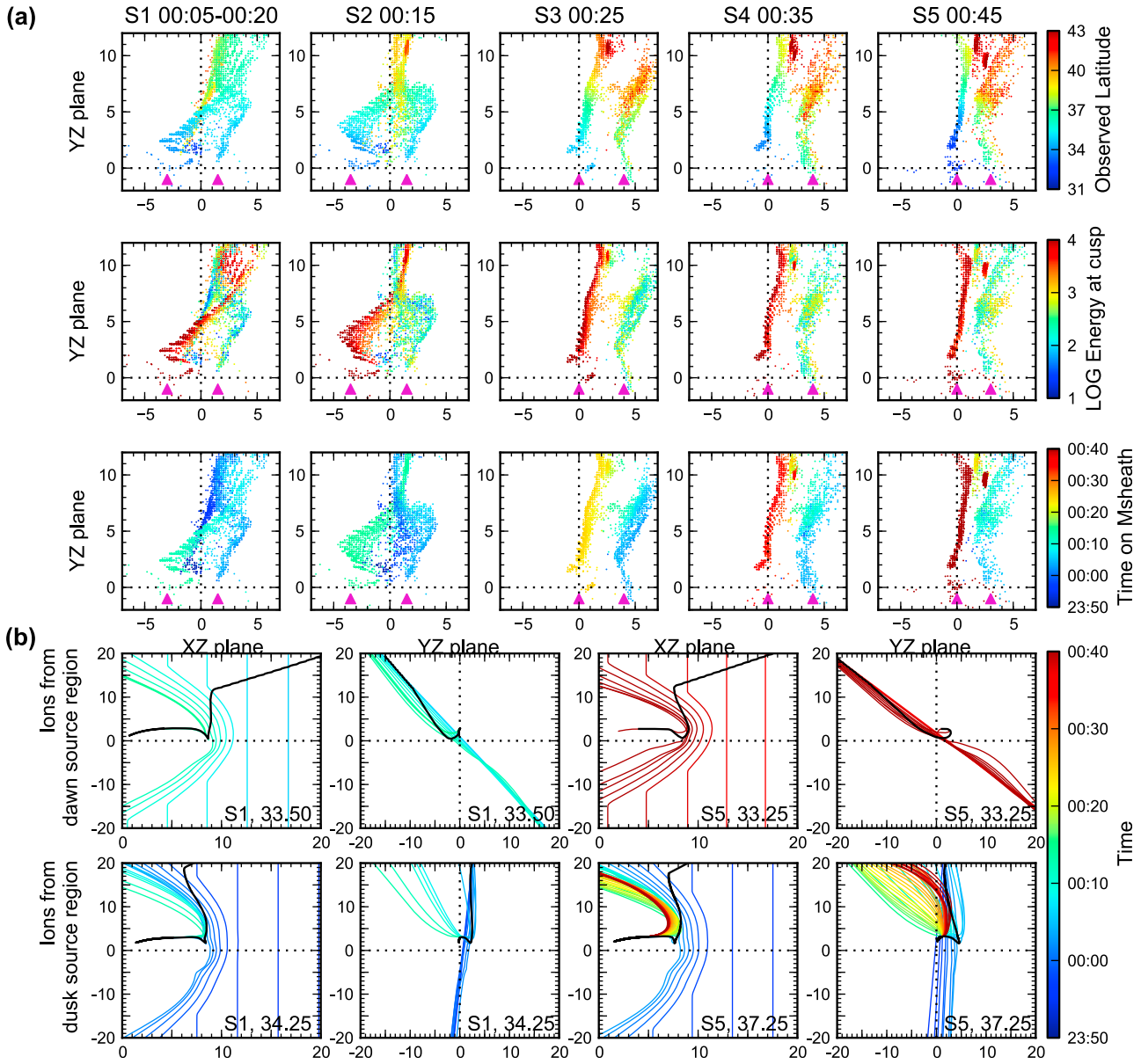

Figure 10. (a) Ion entry points on the magnetosheath plane, projected on the YZ plane as viewed from the Sun. The first to fifth columns show the S1–S5 observations, respectively. The color represents the latitude where the ions are observed, the ion energy at the cusp, and the time when it penetrates the magnetosheath plane. The magenta arrowheads point to two main magnetosheath source regions. (b) Two typical trajectories of ions from each magnetosheath region, projected on the XZ and XY planes. The ions originated from the (top) dawn and (bottom) dusk source regions, respectively. The first and second columns show the ion trajectories observed from S1, and the third and fourth columns show the ones observed from S5. The black lines are ion trajectories, and the colored lines are magnetic field lines that each ion has passed. The color represents the time when the ion passes each field line.

source regions. The trajectories of ions from the duskside source region are aligned with ~180° clock angle, while the trajectories of ions from the dawnside source region are aligned with 140° clock angle. Note that the IMF clock angle changes from 190° to 140° around 00:02 UT (see Figure 7). The two different magnetosheath source regions relate to this IMF clock angle change. The open field lines connect the northern cusp to the duskside magnetosheath during 190° clock angle and the dawnside magnetosheath during 140° clock angle. Therefore, the magnetosheath source region changes from dusk to dawn as the IMF clock angle changes from 190° to 140°.

[63] The dawnside source region of the S3–S5 virtual satellites is located near local noon, not the dawnside

Table 1. Summary of the Model-Observation Comparison[a]

	23 Sep 2004			28 Aug 2003			25 Aug 1998
Comparison Criteria	C4	C1	C3	C1	C3	C4	Polar
1. Dispersion in a correct direction	F	F	F	F	F	F	F
2. Existence of distinct structures	F	F	F	S	S	F	F
3. Slope of dispersion	F	F	F	F	F	F	F
4. Highest energy of dispersed ions	F	F	X	X	X	X	X
Comparison result	Excellent	Excellent	Good	Satisfactory	Satisfactory	Good	Good

[a]F indicates that the model result fulfills the comparison criterion, S indicates that the model result satisfies the criterion with some ambiguity, and X indicates that the model result does not fulfill the criterion.

magnetosheath. However, this region is still located on the dawnside of another source region, the duskside magnetosheath, showing that the magnetosheath source region changes as the IMF clock angle changes. Figure 10a (bottom) shows that ions from the duskside source region still penetrate the magnetosheath plane until 00:10 UT after the IMF clock angle change at 00:02 UT. This is because the magnetopause reconnection process takes time to adjust to the IMF change.

[64] The stepped dispersion observed by Polar is therefore caused by two subsolar reconnection sites before and after the IMF clock angle change. One subsolar reconnection site is located on the duskside magnetopause during 190° IMF clock angle and ceases around 00:10 UT. This reconnection causes ion precipitation from the duskside magnetosheath to the middle and high latitudes of the cusp, producing the low-energy part of the second step and most of the third steps. Another subsolar reconnection site is located on the dawnside magnetopause near local noon during 140° IMF clock angle, and remains active after 00:10 UT. This reconnection causes ion precipitation from both the dawnside magnetosheath and local noon to the low and middle latitudes of the cusp, producing most of the first step and the high-energy part of the second step.

[65] This stepped dispersion is thus a temporal structure in the sense that the two subsolar reconnection sites appear at different times by the change of the IMF clock angle. It is also a spatial structure in the sense that the ions from both reconnection sites are continuously observed for 30 min by our virtual satellites. The ions originating from the ceased reconnection site are low-energy ions, i.e., slow ions which take a long time to travel from the magnetopause to the cusp. This is why our satellites observe these ions for 30 min although the reconnection has already ceased. Thus, this stepped dispersion is of both temporal and spatial nature.

4. Summary and Conclusion

[66] We introduced a new model of cusp ion structures by using the LTPT with the OpenGGCM 3D MHD model. The LTPT is composed of an ion tracer and a density calculator. The ion tracer tracks cusp ions backward in time until they reach the magnetosheath. It integrates the Lorentz equation and the equation of motion with electromagnetic fields obtained from the OpenGGCM simulation. Then, the density calculator computes phase-space densities of the cusp ions at the magnetosheath with their velocities and the velocity distribution in the magnetosheath. By using Liouville's theorem, we map the PSDs in the magnetosheath to the cusp. We calculate the differential flux or energy flux with these PSDs and display the flux on an energy versus time spectrogram in order to produce a cusp ion structure. While the previous models of a cusp ion structure [*Onsager et al.*, 1995; *Wing et al.*, 2001] use empirical electromagnetic field models to trace the cusp ions, our model uses the OpenGGCM MHD model which provides time-dependent electromagnetic fields according to SW-IMF variations. Thus, our model can expand the study of cusp ion structures for dynamic SW-IMF events. The OpenGGCM is also considered to be more realistic in terms of reconnection location and timing, which turns out to be crucial to understand stepped ion structures.

[67] We demonstrate our model's validity by reconstructing the cusp ion structures during three cusp-crossing events of Cluster and Polar satellites. We first define four comparison criteria: (1) the modeled dispersion is in a correct direction, (2) the model reproduces the distinct structures visible in the observation, (3) the slope of modeled dispersion matches with the slope of observed dispersion within a factor of 2, and (4) the highest energies of the modeled and observed dispersions coincide within a factor of 2. We assess the model predictions as being excellent, good, satisfactory, or unsatisfactory on the basis of the number of fulfilled criteria. The summary of the model assessment is shown in Table 1. In spite of the difficulty of locating satellites in the OpenGGCM's cusp, our model produced two excellent, three good, and two satisfactory results.

[68] The comparison result shows that the approach of combining a global fluid model with a test particle tracer and PSD reconstruction is viable. Furthermore, we covered a wide range of possible ion structures, i.e., normal dispersion, reverse dispersion, double dispersions, and stepped dispersion. This gives us confidence that the model includes all the essential physics and can be used for further studies of the properties of cusp ion structures and their relation to magnetopause processes.

[69] We use these three case studies to shed light on the physical processes that lead to the observed ion dispersion. Specifically, we address the question as to whether the dispersed structures are of temporal or spatial nature and where the ions originate. We find the following.

[70] 1. In the 25 September 2004 case, the bump around 15:23 UT observed by several virtual satellites is a temporal structure caused by the sudden increase of solar wind pressure at 15:23 UT.

[71] 2. In the 28 August 2003 case, the double dispersions in the C1 observation are temporal structures caused by various reconnection rates on the duskside flank of magnetopause.

[72] 3. In the 25 August 1998 case, the stepped dispersion observed by Polar is not only spatial but also temporal. This is because two subsolar reconnection sites appear at different times by the temporal change of the IMF clock angle, and because both sites continuously produce overlapping ion precipitation for 30 min.

[73] From the detailed study of ion trajectories, we also find the following.

[74] 1. Although reconnection is the cause of the ions to enter the cusp, most of them cross the magnetopause often far away from the reconnection site, sometimes even in the other hemisphere. In the 28 August 2003 case, the double dispersions observed by S01 are the result of reconnection on the duskside magnetopause. However, ions composing the double dispersions are mostly from the dawnside magnetosheath. In the 25 August 1998 case, the stepped dispersion is the result of two different subsolar reconnection sites, but most ions precipitate from the northern magnetosheath, away from the equatorial plane where the reconnection sites are located.

[75] 2. In addition to dayside reconnection, the magnetic configuration of magnetosheath itself can cause energy dispersion in the cusp ion structure. In the 28 August 2003 case, the second dispersion observed by S07 is composed of ions temporarily trapped in the dawn flank of magnetosheath because of a local minimum in the magnetic field strength. The sunward boundary of dawnside magnetosheath has strong magnetic field strength around 19:15 UT, and therefore, the ions move back and forth between the earthward and sunward boundaries of the magnetosheath until they reach the nightside of earthward boundary where magnetic field is no longer strong enough to repel them.

[76] We have shown our model's ability to produce and investigate temporal and spatial features of cusp ion structures, which relates to the temporal and spatial properties of reconnection. In future work, we will run the OpenGGCM under various solar wind conditions, and analyze various reconnection mechanisms inside the OpenGGCM. Then, we will model cusp ion structures and study how different reconnection processes lead to energy dispersion in the cusp. This will help to gain a comprehensive picture of the relation between a cusp ion structure and dayside reconnection.

[77] **Acknowledgments.** This work was supported by grants ATM-0503189 and ATM-0639658 from the National Science Foundation, grant NNX10AL07G from NASA, and grant C00058 from the Korea Science and Engineering Foundation. We thank C. P. Escoubet for useful discussions.

[78] Masaki Fujimoto thanks the reviewers for their assistance in evaluating this paper.

References

Chapman, S., and V. C. A. Ferraro (1931a), A new theory of magnetic storms: 1. The initial phase, *Terr. Magn. Atmos. Electr.*, *36*(2), 77–97, doi:10.1029/TE036i002p00077.

Chapman, S., and V. C. A. Ferraro (1931b), A new theory of magnetic storms: 1. The initial phase (continued), *Terr. Magn. Atmos. Electr.*, *36*(3), 171–186, doi:10.1029/TE036i003p00171.

Cowley, S. W. H. (1982), The causes of convection in the Earth's magnetosphere: A review of developments during the IMS, *Rev. Geophys.*, *20*(3), 531–565, doi:10.1029/RG020i003p00531.

Dungey, J. W. (1958), *Cosmic Electrodynamics*, Cambridge Univ. Press, New York.

Dungey, J. W. (1961), Interplanetary magnetic field and the auroral zones, *Phys. Rev. Lett.*, *6*, 47–48, doi:10.1103/PhysRevLett.6.47.

Escoubet, C. P., et al. (2008a), Two sources of magnetosheath ions observed by Cluster in the mid-altitude polar cusp, *Adv. Space Res.*, *41*, 1528–1536, doi:10.1016/j.asr.2007.04.031.

Escoubet, C. P., et al. (2008b), Effect of a northward turning of the interplanetary magnetic field on cusp precipitation as observed by Cluster, *J. Geophys. Res.*, *113*, A07S13, doi:10.1029/2007JA012771.

Escoubet, C. P., et al. (2008c), Ion energy steps observed by Cluster multipoint mission in the polar cusp: Similarity and differences, *Eos Trans. AGU*, *89*(53), Fall Meet. Suppl., Abstract SM54A-07.

Gosling, J. T., M. F. Thomsen, S. J. Bame, T. G. Onsager, and C. T. Russell (1990), The electron edge of low-latitude boundary layer during accelerated flow events, *Geophys. Res. Lett.*, *17*(11), 1833–1836, doi:10.1029/GL017i011p01833.

Hill, T. W., and P. H. Reiff (1977), Evidence of magnetospheric cusp proton acceleration by magnetic merging at the dayside magnetopause, *J. Geophys. Res.*, *82*(25), 3623–3628, doi:10.1029/JA082i025p03623.

Lockwood, M., and M. F. Smith (1989), Low-altitude signatures of the cusp and flux transfer events, *Geophys. Res. Lett.*, *16*(8), 879–882, doi:10.1029/GL016i008p00879.

Lockwood, M., and M. F. Smith (1990), Reply to "Comment on 'Low-altitude signatures of the cusp and flux transfer events,' " *Geophys. Res. Lett.*, *17*(3), 305–306, doi:10.1029/GL017i003p00305.

Lockwood, M., and M. F. Smith (1994), Low and middle altitude cusp particle signatures for general magnetopause reconnection rate variations: 1. Theory, *J. Geophys. Res.*, *99*(A5), 8531–8553, doi:10.1029/93JA03399.

Onsager, T. G., S.-W. Chang, J. D. Perez, J. B. Austin, and L. X. Janoo (1995), Low-altitude observations and modeling of quasi-steady magnetopause reconnection, *J. Geophys. Res.*, *100*(A7), 11,831–11,843, doi:10.1029/94JA02702.

Peroomian, V. (1994), Large scale kinetic modeling of magnetospheric plasma, PhD thesis, Univ. of Calif., Los Angeles.

Peroomian, V., M. El-Alaoui, M. Ashour-Abdalla, and L. M. Zelenyi (2006), Dynamics of ionospheric O^+ ions in the magnetosphere during the 24–25 September 1998 magnetic storm, *J. Geophys. Res.*, *111*, A12203, doi:10.1029/2006JA011790.

Raeder, J. (2003), Global magnetohydrodynamics: A tutorial, in *Space Plasma Simulation*, *Lect. Notes Phys.*, vol. 615, edited by J. Büechner, C. T. Dum, and M. Scholer, pp. 212–246, Springer, New York.

Raeder, J., J. Berchem, and M. Ashour-Abdalla (1998), The geospace environment modeling grand challenge: Results from a Global Geospace Circulation Model, *J. Geophys. Res.*, *103*(A7), 14,787–14,797, doi:10.1029/98JA00014.

Raeder, J., R. L. McPherron, L. A. Frank, S. Kokubun, G. Lu, T. Mukai, W. R. Paterson, J. B. Sigwarth, H. J. Singer, and J. A. Slavin (2001), Global simulation of the Geospace Environment Modeling substorm challenge event, *J. Geophys. Res.*, *106*(A1), 381–395, doi:10.1029/2000JA000605.

Reiff, P. H., T. W. Hill, and J. L. Burch (1977), Solar wind plasma injection at the dayside magnetospheric cusp, *J. Geophys. Res.*, *82*(4), 479–491, doi:10.1029/JA082i004p00479.

Rème, H., et al. (2001), First multispacecraft ion measurements in and near the Earth's magnetosphere with the identical Cluster ion spectrometry (CIS) experiment, *Ann. Geophys.*, *19*, 1303–1354, doi:10.5194/angeo-19-1303-2001.

Rosenbauer, H., H. Grünwaldt, M. D. Montgomery, G. Paschmann, and N. Sckopke (1975), HEOS 2 plasma observations in the distant polar magnetosphere: The plasma mantle, *J. Geophys. Res.*, *80*(19), 2723–2737, doi:10.1029/JA080i019p02723.

Ruohoniemi, J. M., and R. A. Greenwald (1996), Statistical patterns of high-latitude convection obtained from Goose Bay HF radar observations, *J. Geophys. Res.*, *101*(A10), 21743–21763, doi:10.1029/96JA01584.

Shelley, E. G., R. D. Sharp, and R. G. Johnson (1976), He^{++} and H^+ flux measurements in the dayside cusp: Estimates of convection electric field, *J. Geophys. Res.*, *81*(13), 2363–2370, doi:10.1029/JA081i013p02363.

Shelley, E. G., et al. (1995), The Toroidal Imaging Mass-Angle Spectrograph (TIMAS) for the Polar mission, *Space Sci. Rev.*, *71*, 497–530, doi:10.1007/BF00751339.

Smith, M. F., and M. Lockwood (1996), Earth's magnetospheric cusps, *Rev. Geophys.*, *34*(2), 233–260, doi:10.1029/96RG00893.

Stern, D. P. (1985), Parabolic harmonics in magnetospheric modeling: The main dipole and the ring current, *J. Geophys. Res.*, *90*(A11), 10,851–10,863, doi:10.1029/JA090iA11p10851.

Trattner, K. J., S. A. Fuselier, W. K. Peterson, M. Boehm, D. Klumpar, C. W. Carlson, and T. K. Yeoman (2002), Temporal versus spatial

interpretation of cusp ion structures observed by two spacecraft, *J. Geophys. Res.*, *107*(A10), 1287, doi:10.1029/2001JA000181.

Trattner, K. J., S. A. Fuselier, S. M. Petrinec, T. K. Yeoman, C. Mouikis, H. Kucharek, and H. Rème (2005), The reconnection sites of spatial cusp structures, *J. Geophys. Res.*, *110*, A04207, doi:10.1029/2004JA010722.

Trattner, K. J., S. A. Fuselier, S. M. Petrinec, T. K. Yeoman, C. P. Escoubet, and H. Rème (2008), The reconnection site of temporal cusp structures, *J. Geophys. Res.*, *113*, A07S14, doi:10.1029/2007JA012776.

Tsyganenko, N. A., and D. P. Stern (1996), Modeling the global magnetic field of the large-scale Birkeland current systems, *J. Geophys. Res.*, *101*(A12), 27,187–27,198, doi:10.1029/96JA02735.

Wing, S., P. T. Newell, and J. M. Rouhoniemi (2001), Double cusp: Model prediction and observational verification, *J. Geophys. Res.*, *106*(A11), 25,571–25,593, doi:10.1029/2000JA000402.

H. J. Connor and J. Raeder, Space Science Center, University of New Hampshire, 8 College Rd., Durham, NH 03824, USA. (hjkim@artemis.sr.unh.edu; j.raeder@unh.edu)

K. J. Trattner, Lockheed-Martin Advanced Technology Center, B255, L9-42, 3251 Hanover St., Palo Alto, CA 94304-1191, USA.